Unveiling the origins of high ionic conductivity in lithium phosphorus oxynitride amorphous electrolytes

Annie-Kim Landry, Racha Bayzou, Anass Benayad, Julien Trébosc, Frédérique Pourpoint, Olivier Lafon, Frédéric Le Cras, Brigitte Pecquenard, Rafael Bianchini Nuernberg

Unveiling the origins of high ionic conductivity in lithium phosphorus oxynitride amorphous electrolytes

Annie-Kim Landry[1,2], Racha Bayzou[3], Anass Benayad[4], Julien Trébosc[3], Frédérique Pourpoint[5], Olivier Lafon[5], Frédéric Le Cras[1], Brigitte Pecquenard Le Cras[2#], Rafael B. Nuernberg[2]*

[1] Univ. Grenoble Alpes, CEA, LITEN, DEHT, 38000 Grenoble, France

[2] Univ. Bordeaux, CNRS, Bordeaux INP, ICMCB, UMR 5026, 33600 Pessac, France

[3] Univ. Lille, CNRS, INRAE, Centrale Lille, Univ. Artois, FR 2638 – IMEC – Fédération Chevreul, 59000 Lille, France

[4] Univ. Grenoble Alpes, CEA, LITEN, DTNM, 38000 Grenoble, France

[5] Univ. Lille, CNRS, Centrale Lille, Univ. Artois, UMR 8181 – UCCS – Unité de Catalyse et Chimie du Solide, 59000 Lille, France

Abstract

Lithium phosphorus oxynitride, having an amorphous structure, has been enabling all-solid-state thin film batteries with lithium metal anode and high-voltage cathodes since the nineties. Nevertheless, the origins of its outstanding ionic conductivity compared to its crystalline counterparts as well as the interplay between structure and ionic transport in this electrolyte have remained elusive. Herein, we have applied a compelling methodology based on impedance spectroscopy analyses to isolate the distinct energetic contributions for the ionic conduction process namely, the enthalpies for defect formation and migration. The variations of these enthalpies with nitrogen content are correlated with structural aspects unveiled by solid-state nuclear magnetic resonance (NMR) and depth profiling X-ray photoelectron spectroscopies. The main findings indicate that the amorphous structure, inherent to radiofrequency magnetron sputtering synthesis, is the root of a striking decrease of the enthalpy related to defect formation while the nitrogen incorporation plays a crucial role in Li^+ ions mobility by forming bridging species, which tend to lower the enthalpy of migration.

*corresponding author

Rafael Bianchini Nuernberg : *rafael.bianchini_nuernberg@bordeaux-inp.fr*

in memoriam Brigitte Pecquenard Le Cras deceased 18 Septembre 2022

1 Introduction

Lithium phosphorus oxynitride (LiPON) solid electrolytes, having an amorphous structure, were first synthesized at the Oak Ridge National Laboratory in the 1990s employing radiofrequency (RF) magnetron sputtering [1,2]. Research on this compositional system was motivated by the development of all-solid-state lithium microbatteries, which can be used for many applications in the fields of communication, the internet of things, microactuators or implantable biosensors [3]. Despite its moderate room temperature ionic conductivity ($>10^{-6}$ S.cm^{-1}), thin film processing techniques enable reduced thickness (around 1 µm) resulting in ionic resistance compatible to microbattery applications [1,2,4–6]. Additionally, LiPON thin films have emerged as a promising candidate as a protective layer for negative electrodes in all-solid-state bulk batteries [7–9], including lithium metal (Li) [7,8]. Strictly speaking, LiPON is not thermodynamically stable against Li, presenting a decomposition potential of 0.7 V vs Li/Li$^+$ as predicted by first-principles calculations [10] and confirmed through experimental studies employing in-situ X-ray photoelectron (XPS) spectroscopy [11] and cryogenic electron microscopy [12]. Nevertheless, ultimate decomposition products comprising Li_3N, Li_3P and Li_2O, enable the formation of a very thin (~10nm) [13] and efficient passivating layer, which inhibits further decomposition [10,11]. Besides, its low electronic conductivity ($<10^{-10}$ S.cm^{-1}) [6,14] and the absence of grain boundaries [15–17] are well-suited for solid electrolyte applications. These combined characteristics contribute in large part to its resistance to lithium penetration and dendrite propagation [18], which ultimately results in outstanding cycling performance with 90% capacity retention after 10 000 cycles [19].

LiPON thin films are commonly prepared from a Li_3PO_4 target by RF magnetron reactive sputtering under nitrogen rich atmosphere [1,20–24]. The relationships between sputtering conditions, chemical composition, local structure, and ionic conductivity of LiPON thin films have been

extensively explored and reported in literature [17,21,22,24]. Based on the general composition $Li_xPO_yN_z$, where $x + 5 = 2y + 3z$, a wide range of compositions can be obtained by varying sputtering conditions [20–22]. It is commonly acknowledged that the ionic conductivity can be enhanced by increasing the N/P ratio if the Li/P ratio of three is at least roughly preserved [1,20,22]. Nevertheless, the resulting local structure once nitrogen is incorporated and the structural role of the latter regarding the ionic transport are still debated [22,25–27]. The most abundant source of evidence regarding the structural features of LiPON thin films stems from XPS analysis. Indeed, N1s core peak spectra have generally been decomposed into two main contributions, namely, doubly (N_d) and triply coordinated (N_t) by P atoms [1,21–24]. While confirming the presence of N_d units, molecular dynamics simulations have proposed the preferred formation of isolated PO_3N unit or apical (N_a) instead of the N_t configuration evidenced by XPS [26,28,29]. Recent 1D and 2D solid-state nuclear magnetic resonance (NMR) experiments on RF-sputtered LiPON have finally corroborated the existence of N_a and N_d species [27,30]. Regarding the structural role of nitrogen on the ionic transport of these electrolytes, computational studies have suggested that the incorporation of nitrogen as N_d in $[O_3PNPO_3]^{5-}$ units should favors Li^+ mobility by decreasing Li^+-anions attractive interactions [26,29]. Meanwhile, experimental studies focusing on ionic transport mechanisms suggested that only a part of Li^+ ions are involved in the conduction process and that the charge carrier concentration barely change with temperature, leading to the conclusion that the ionic transport should be mainly governed by an increase of the mobility [14,22].

Despite numerous comprehensive investigations into the structural aspects and electrical properties of LiPON amorphous electrolyte, the relationship between them remains vaguely understood. Hence, the primary objective of this paper is to provide further insights into the interplay between chemical composition, local structure, and ionic transport in this system. For that purpose, LiPON thin films with various N contents were prepared by RF magnetron sputtering by

tuning plasma conditions inside the chamber. The effects of composition variations on the local structure were then investigated by combining two complementary techniques, namely, XPS depth profiling and solid-state NMR spectroscopy. Moreover, impedance and permittivity analyses were combined to discriminate the enthalpic contributions arising from defect formation and ion migration. Finally, the variation of these enthalpies with nitrogen content is interpreted in the light of unique structural features of LiPON thin films such as their amorphous structure and the formation of dimers caused by nitrogen incorporation.

2 Experimental procedure

2.1 Synthesis

Lithium phosphorus oxide (LiPO) and oxynitride (LiPON) thin films were deposited by RF magnetron sputtering from a γ-Li_3PO_4 target in a chamber (Plassys) connected to an argon-filled glove box. To prepare the target, β-Li_3PO_4 (Sigma Aldrich, 99.9%) powder was annealed at 923 K for 12 h under argon to obtain γ-Li_3PO_4 phase. A 50 mm diameter target was then prepared by spark plasma sintering (SPS) from this powder [30]. The resulting γ-Li_3PO_4 target was translucent, with an overall density of 2.33 g.cm^{-3} corresponding to a relative density of about 99%. Before each deposition, the chamber was pumped until the pressure was less than 5×10^{-5} Pa and a pre-sputtering was systematically performed during at least 30 min. All thin films were deposited with a nominal RF power density of 2 W.cm^{-2} and a target-substrate distance equal to 80 mm. No intentional heating nor DC bias were applied to the substrate during deposition. LiPO films were prepared with a total pressure of 1 Pa under pure argon atmosphere (50 ml.min^{-1} gas flow), while LiPON films were deposited under pure nitrogen atmosphere by varying the flow rate (2, 20 and 40 ml.min^{-1}). The deposition rates were estimated to be about 0.15 μm.h^{-1} by measuring the

thickness using a profilometer Tencor Alpha-Step 200. Different substrates were used for film deposition depending on the envisaged characterization. All samples were handled in an argon-filled glove box and transferred to the different devices used for characterization through airtight containers.

2.2 Chemical analyses

P, N and O contents were determined by means of electron probe micro-analysis (EPMA) employing a CAMECA SX100 equipment. For EPMA, LiPO(N) samples were produced by sputtering thin films of about 1 µm on Si_3N_4 substrate previously covered with a gold coating. The thin films are covered with a 20 nm thickness gold layer to ground the sample and analyzed by applying a 10 kV excitation voltage, which was carefully chosen to maximize the depth of analysis without reach the Si_3N_4 substrate. InP, Si_3N_4 and $Y_3Fe_5O_{12}$ compounds were used as calibration standards. The Li and P contents were determined using an inductively coupled plasma-optical emission spectrometer (ICP-OES) model Varian 720ES. Solutions for ICP-OES analyses were prepared by digesting the thin films deposited on a glass substrate in a boiling solution of diluted HCl. Then, demineralized water was added to reach concentrations between 3 and 14 $mg.L^{-1}$. Five measurements were performed for each sample injecting each time about 5 ml of the solution. Emission line wavelength of 610.365 nm and 214.914 nm were respectively chosen for Li and P elements. The results of EPMA and ICP-OES were combined to determine the full elemental composition.

2.3 Structural Characterization

Local environments of P and Li atoms in the prepared LiPON samples were respectively probed using ^{31}P and ^{7}Li solid-state NMR spectroscopy. To enable further recovery of LiPO(N) thin film samples, silicon substrates were previously coated with a polymer thin film. Polyvinylidene difluoride (PVDF) was chosen due to its composition, which is free from any elements present in the LiPO(N) film. To this end, 20 g of PVDF (Sigma Aldrich, molecular weight of 534,000 u) were dissolved in 80 g of N-methyl-2-pyrrolidone under agitation at 353 K for 12 h in a hermetic glass container. Spin coating was performed on a Specialty Coating Systems G3 equipment with a rotation speed of 4000 rpm during 45 s employing 4 ml of the polymer solution. The film was then dried at 423 K on a hot plate for 60 s, resulting in a PVDF coating of a few microns. In order to achieve a good NMR signal-to-noise ratio (SNR), about 2.5 µm of LiPO and LiPON were deposited on the PVDF layer, which correspond to roughly 16 h of deposition. The samples were finally collected by scratching the surface of the Si substrate with a cutter in a glovebox and about 1 mg of the resulting powder, composed of LiPON and PVDF, was introduced in a 2.5 mm rotor using silicone inserts to center the sample in the middle of the detection coil [30].

Both ^{31}P and ^{7}Li nuclei have moderate gyromagnetic ratios, $\gamma(^{31}P)/\gamma(^{1}H) \approx 0.405$ and $\gamma(^{7}Li)/\gamma(^{1}H) \approx 0.389$ and high natural abundance, *NA* = 100 and 92.41% for ^{31}P and ^{7}Li, respectively. Furthermore, ^{31}P nuclei have a nuclear spin value $I = 1/2$, whereas ^{7}Li is a spin-3/2 isotope, usually subject to small quadrupolar interaction. Therefore, ^{31}P and ^{7}Li NMR spectra were acquired at a static magnetic field $B_0 = 9.4$ T on a Bruker BioSpin Avance NEO NMR spectrometer equipped with 2.5 mm triple resonance HXY probe spinning at a MAS frequency, $\nu_R = 25$ kHz. ^{31}P and ^{7}Li NMR experiments were carried out using $\pi/2$ pulse lengths of 2.05 and 1.80 µs, respectively. Quantitative one-dimensional (1D) ^{31}P and ^{7}Li NMR spectra under magic-angle spinning (MAS)

conditions were acquired using Bloch-decay experiment. The recovery delays, τ_{RD}, were equal to five times the longest longitudinal relaxation time, T_1, to ensure quantitative NMR measurements. The 1D ^{31}P and ^{7}Li NMR spectra resulted from averaging 256 and 128 transients with τ_{RD} = 40-70 s (depending on the sample) and 5 s, leading to total experimental times of 3-5 h and 11 min, respectively. The ^{31}P and ^{7}Li isotropic chemical shifts, δ_{iso}, were referenced to 85 wt% H_3PO_4 and 1 mol.L^{-1} LiCl aqueous solutions, respectively. 1D ^{31}P MAS NMR spectra were simulated using dmfit software [31] as the sum of four Gaussian line shapes since the amorphous structure of LiPON results in a distribution of ^{31}P local environments and hence, of isotropic chemical shifts, $\delta_{iso}(^{31}P)$. The $\delta_{iso}(^{31}P)$ values and full-width at half maximum (FWHM) of each site were equal to those recently measured for LiPON thin films prepared by RF sputtering with a nitrogen flow rate of 40 ml.min^{-1} [30]. These NMR parameters were kept constant for all samples and only intensities were adjusted.

XPS depth-profiling analyses were carried out using a ULVAC-PHI VersaProbe II spectrometer. Samples were produced by sputtering thin films of about 1 μm directly on commercial Si wafer substrates. Measurements were performed under ultra-high vacuum ($p < 5.10^{-7}$ Pa) with a micro-focused (beam size diameter of 100 μm) AlKα X-ray beam (photon energy of 1486.6 eV) and a radiation power of 25 W. The take-off angle for photoelectron detection was 45°. All experiments were performed with both electron and Ar-ion charge neutralization systems on. High-resolution spectra were measured with a pass energy of 23 eV, corresponding to an energy resolution of about 0.6 eV, as estimated from the FHWM of the Ag3d$_{5/2}$ spectra of an Ag reference sample. Argon gas cluster ion beam etching (GCIB) was carried out in order to remove surface contamination without damaging its structure and have access to the bulk chemical structure. A cluster size of 2500 atoms accelerated to 10 kV is employed which is equivalent to 4 eV/atoms. Spectra were recorded at the

surface before GCIB etching and in the bulk after distinct duration of GCIB etching. Peak fitting was carried out using the MultiPak data analysis software and employing a Pseudo-Voigt function as peak shape.

2.5 Electrical Characterization

The electrical behavior of LiPO(N) thin films was characterized by electrochemical impedance spectroscopy (EIS). EIS measurements were performed on Au (~100 nm) / LiPON (~1 μm) / Au (100 nm) stacks deposited on a glass substrate, and which have 4 mm^2 active surface area (Figure S1). Patterning of the three layers is achieved using stainless steel shadow masks and allows to prepare simultaneously four identical cells. This configuration allows therefore to carry out multiple measurements for each thin film electrolyte to ensure the reproducibility [22]. The precise thickness of LiPO(N) thin films was measured in the vicinity of the gold electrodes employing a Tencor profilometer Alpha-Step 200. EIS measurements were performed employing a Solartron 1260 Impedance/Gain Phase Analyzer in the frequency range between 1 MHz and 1 Hz, with an applied root mean square voltage of 50 mV, 30 points per decade and 20 measures per point. The measurements were carried out under Ar, in an airtight cell, from 298 to 348 K and every 5 K.

3 Results and Discussion

3.1 Chemical composition and local structure of LiPON thin films

LiPON thin films samples were named as LiPONz, where *z* is the nitrogen volumetric flow rate used to prepare them. Table 1 summarizes the different samples prepared with various gas flows and their respective chemical compositions determined by combining ICP-OES and EPMA analyses. As expected, increasing nitrogen flow rate results in higher N/P and lower O/P ratios

since nitrogen atoms should substitute oxygen ones. The enhancement of the N content as a function of the N_2 gas flow is more substantial up to 20 ml/min. This overall behavior has been also highlighted in our previous study [22], leading to the conclusion that the incorporation of nitrogen might reach a saturation point. Conversely, the Li/P cationic ratio remains nearly constant, close to the value in lithium orthophosphate (Li/P ~ 3), regardless of the nitrogen incorporation. Since it is expected that the lithium content might also impact the ionic conductivity, a rather constant Li/P ratio as a function of nitrogen incorporation is ideal to evaluate the structural effect of nitrogen on the ionic transport properties of these LiPON thin films.

Table 1 - Chemical compositions of LiPO(N) thin films prepared with different gas flows. Li/P ratios are determined from ICP-OES analyses while O/P and N/P ratios are measured by EPMA.

Samples	Gas flow ($ml.min^{-1}$)	ICP	EPMA		Chemical Composition
		Li/P	O/P	N/P	
LiPO	50 Ar	2.9(2)	4.3(1)	0	$Li_{2.9}PO_{4.3}$
LiPON2	2 N_2	3.2(2)	3.5(1)	0.25(3)	$Li_{3.2}PO_{3.5}N_{0.25}$
LiPON20	20 N_2	3.1(2)	3.0(1)	0.57(3)	$Li_{3.1}PO_{3.0}N_{0.57}$
LiPON40	40 N_2	3.2(2)	3.0(1)	0.68(3)	$Li_{3.2}PO_{3.0}N_{0.68}$

Figure 1 displays the 1D ^{31}P NMR spectra of the investigated LiPO and LiPON samples. The spectrum of LiPO can be simulated as a single signal assigned to PO_4^{3-} orthophosphate units (denoted Q_0^0). On the other hand, the spectra of LiPON samples are the sum of several overlapping ^{31}P signals which are deconvoluted into four distinct peaks resonating at 19.4, 13.9, 9.7 and 4.7

ppm. These peaks are respectively assigned to Q^0_1, Q^1_1, Q^0_0 and Q^1_0 P sites, where Q^n_m denotes P sites covalently linked to *n* bridging atoms and *m* nitrogen atoms. Therefore, Q^0_0 and Q^1_0 P sites correspond respectively to orthophosphate PO_4^{3-} and $[O_3POPO_3]^{4-}$ pyrophosphate anions, respectively, whereas, Q^0_1 and Q^1_1 P sites are present in PO_3N^{4-} isolated tetrahedra containing N_a sites and $[O_3PNPO_3]^{5-}$ dimers containing N_d sites, respectively. This assignment is based on a structural model developed for LiPON thin films prepared by RF sputtering, which has been recently proposed based on *ab initio* molecular dynamics, density functional theory (DFT) calculations of NMR parameters and solid-state NMR measurements of ^{31}P chemical shift anisotropy as well as ^{31}P-^{31}P and ^{31}P-^{14}N dipolar couplings [27]. The best-fit parameters[30] to simulate the 1D ^{31}P MAS spectra of Figure 1 are given in Table 2. Overall, the most significant structural variation spotted with the gradual nitrogen incorporation is the increase of $[O_3PNPO_3]^{5-}$ dimers containing N_d sites (Q^1_1) at the expense of PO_4^{3-} isolated tetrahedra (Q^0_0). However, it is also important to note the emergence and the slight increase of $[O_3POPO_3]^{4-}$ dimers (Q^1_0) with the nitrogen incorporation as well as the nearly constant concentration of isolated PO_3N^{4-} tetrahedra containing N_a sites (Q^0_1) in all LiPON thin films. Ultimately, two others structural parameters of relevance can be derived from the analyses of 1D ^{31}P MAS spectra: the overall dimer concentration (P_d/P), which gives an idea of the degree of dimerization of the amorphous structure; and the ratio of nitrogen sites forming dimers regarding the overall (N_d/N), providing a picture of the distribution of nitrogen atoms in the N_d and N_a sites.

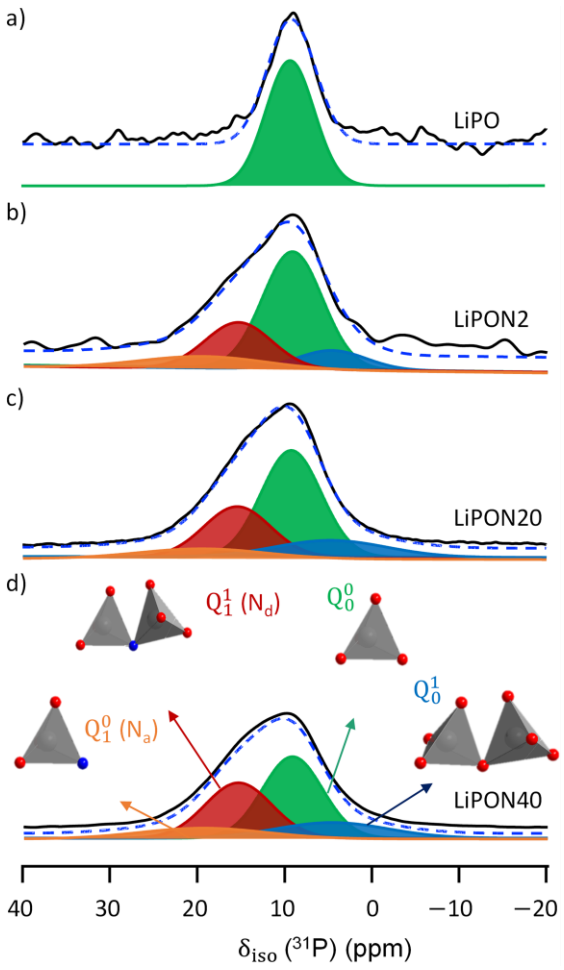

Figure 1 - Experimental and simulated quantitative 1D ^{31}P MAS NMR spectra of (a) LiPO, (b) LiPON2, (c) LiPON20 and (d) LiPON40 at 9.4 T with a MAS frequency of 25 kHz. The spectra of LiPON samples were adjusted as the sum of four distinct signals assigned to Q^0_1, Q^1_1, Q^0_0 and Q^1_0 P sites by order of decreasing isotropic chemical shift, whereas the spectrum of LiPO was simulated as a single signal assigned to Q^0_0 site.

Table 2 - Parameters used to simulate the 1D ^{31}P MAS NMR spectra of LiPO, LiPON2, LiPON20 and LiPON40 shown in Figure 1.

Site		Q_1^0	Q_1^1	Q_0^0	Q_0^1	P_d/P	N_d/N
Species		PO_3N^{4-}	$[O_3PNPO_3]^{5-}$	PO_4^{3-}	$[O_3POPO_3]^{4-}$	$\frac{Q_1^1+Q_0^1}{Q_1^0+Q_1^1+Q_0^0+Q_0^1}$ [b]	$\frac{\frac{Q_1^1}{2}}{\frac{Q_1^1}{2}+Q_1^0}$ [c]
δ_{iso} (^{31}P) (ppm)		19.4(3)	13.9(2)	9.7(1)	4.7(3)		
FWHM (ppm)		10.6(4)	10.8(3)	10.0(2)	15.0(4)		
Fractions /% [a]	LiPO	0	0	100	0	0	-
	LiPON2	12(6)	16(4)	66(3)	5(8)	22.1	40.5
	LiPON20	12.0(7)	20.9(5)	59.6(3)	8(1)	28.5	46.5
	LiPON40	12.6(4)	27.3(2)	50.1(2)	9.9(3)	37.2	52.0

[a] These fractions were determined from the relative integrated intensities of signals in the quantitative 1D ^{31}P NMR spectra of Figure 1 and correspond to fractions of P atoms located in Q_m^n sites with respect to the total number of P atoms. [b] Equation used to calculated P_d/P ratio, where Q_m^n denotes the fraction of P atoms in that site. [c] Equation used to calculate N_d/N ratio from the fractions of Q_1^1 and Q_1^0 sites.

Whereas 1D ^{31}P solid-state NMR spectra probe the presence of N_a sites besides the N_d local environment, several structural studies by XPS on LiPON amorphous thin films evidenced the presence of triply coordinated sites instead (N_t) [1,21–24]. Similar contradictions have been reported in literature when confronting XPS surface analyses with other characterization techniques based on bulk analyses. This led authors to question the representativeness of the surface regarding the bulk of these thin films, specially knowing their intrinsic reactivity [28,32]. In this sense, XPS depth-profiling analyses can be particularly insightful since it can probe the local structure at different depths in the sample. Figure 2 shows depth-profiling N1s core level spectra recorded at the surface and down towards the bulk (after GCIB etching) of the LiPON2, LiPON20 and LiPON40 thin films. At the surface, it is highlighted the presence of three nitrogen environments characterized by the peaks at 397.4 (Pk1), 398.8 (Pk2) and 403.2 eV (Pk3) (Figure 2b), commonly assigned respectively to N_d, N_t [1,21–24] and NO_2 [23]. The presence of NO_2 at the surface of LiPON thin films

already indicates the partial oxidation of the extreme surface. It is interesting to note that this surface degradation occurs despite of the careful and airtight manipulation of the samples. Conversely, when etching is carried out, allowing to access the structure down to the bulk (Figure 2c), the NO_2 contribution tends to disappear and the middle energy peak usually assigned to N_t (398.8 eV) is mostly suppressed. This result should close the controversial debate about these N_t species [1,21–24], since it clearly demonstrates that these latter are mostly restricted to the extreme surface of the material, and therefore should not play a major role in the mechanism of Li^+ conduction. Their presence would highlight the reactivity of LiPON thin films or the metastable character of the amorphous material. Therefore, the main N1s peak (Pk1) observed for the bulk of the samples could be assigned to both N_d sites forming $[O_3PNPO_3]^{5-}$ dimers and N_a sites located on isolated PO_3N^{4-} tetrahedra (Figure 2b), in accordance with the NMR results. Indeed, by computing core-level binding energies of crystalline structural models base on $Li_xPO_yN_z$ compositional system, it was evidenced that N_a sites should present lower but very close N1s core-level binding energy of those expected for N_d sites [28,33,34]. Besides, the introduction of N_a sites in the model has shown to affect the core-level binding energy of N_d sites, which increases the complexity for developing realistic structural models to properly calculate N1s core-level binding energies on these systems [33,34]. P 2p core-level spectra recorded at the surface and down to the bulk of LiPON thin films also reveal structural differences between surface and bulk. Spectra recorded at the surface show two $P2p_{3/2-1/2}$ doublets at around 134.2-135.0 and 133.0-133.8 eV noted as Pk1 and Pk2, respectively. In the bulk, an additional doublet at 131.8-132.6 eV (Pk3) is necessary to successfully fit the experimental data (Figure S2). Pk1 and Pk2 can be respectively assigned to P-O and P-N_d interactions [33,34] while the Pk3 could arise from P-N_a interactions that are not present in the surface due to the oxidation N_a species leading to the formation of NO_2.

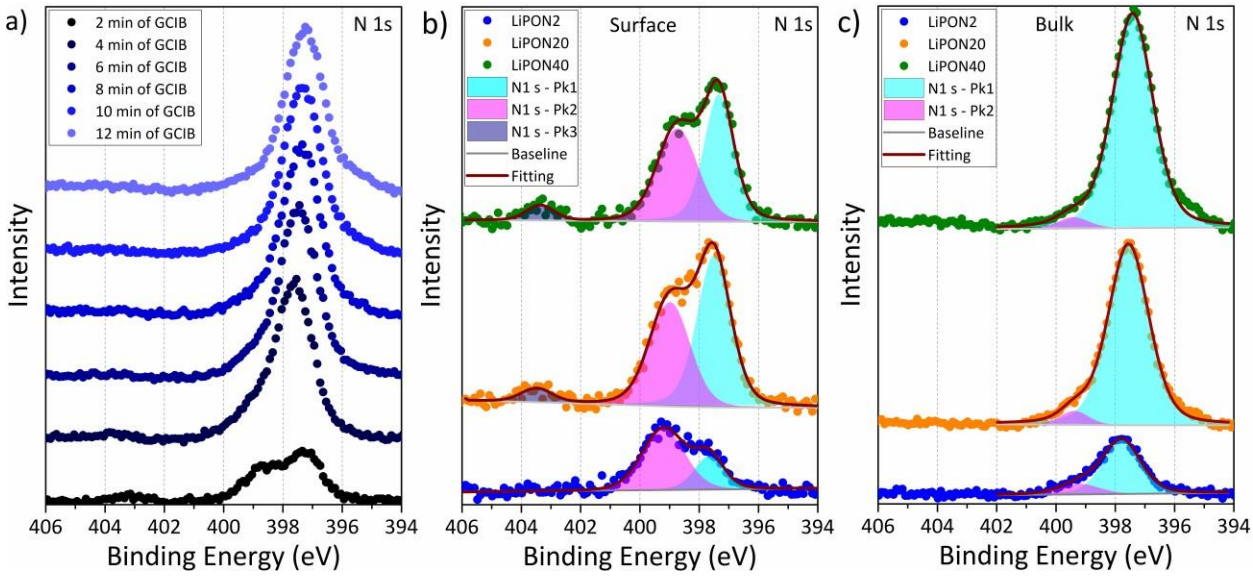

Figure 2 - High-resolution N1s core level spectra of (a) LiPON40 at distinct depths after different durations of GCIB etching (indicated on the figure) and of (b) the surface and (c) the bulk of LiPON2, LiPON20 and LiPON40 samples along with their deconvolution. The spectra of the surface and the bulk were recorded before and after GCIB etching of 10 min, respectively.

Moreover, the coexistence of N_a and N_d species are in good agreement with the experimental chemical composition of these LiPON thin films. Considering that the Li/P ratio is constrained around three by the initial composition of the target (Li_3PO_4), the incorporation of every two nitrogen atoms has to be followed by the release of three oxygens if the electroneutrality is maintained. Besides, since the initial orthophosphate structure of the target comprises solely non-bridging oxygens, the incorporation of nitrogen as N_a, N_d and N_t species will lead to distinct degree of polymerization of the structure and cause varied charge balance scenarios according to the following reasonings:

i. the formation of N_a takes place through the simple substitution of <u>one</u> O^{2-} by <u>one</u> N^{3-} ($O^{2-} \leftrightarrow N^{3-} + Li^{+}$), leading to a overall unbalanced charge that has to be compensated with the <u>addition</u> of <u>one</u> Li^{+}.

ii. the formation of N_d sites will form a phosphate dimmer and requires the substitution of <u>two</u> O^{2-} for each N^{3-} incorporate ($2O^{2-} + Li^{+} \leftrightarrow N^{3-}$), which must be charge-balanced by the <u>removal</u> of <u>one</u> Li^{+}.

iii. the formation of N_t sites will form a phosphate network node and requires the substitution of <u>three</u> O^{2-} for each N^{3-} incorporated ($3O^{2-} + 3Li^{+} \leftrightarrow N^{3-}$), leading to the <u>removal</u> of <u>three</u> Li^{+} to preserve electroneutrality.

Consequently, if the Li/P ratio of the initial orthophosphate structure is preserved, electroneutrality entails that the fraction of nitrogen distributed in the different possible sites is given by $\frac{N_a}{N} = \frac{N_d}{N} + \frac{3N_t}{N}$. Therefore, the formation of only N_a and N_d species under the same proportion is enough to maintain the Li/P ratio around three while the formation of N_a and N_t alone is just feasible if three times more N_a is formed than N_t. Since the Li/P ratio in these LiPO(N) thin films is close to three, it is unlikely to form mostly N_t species since it would be followed by a strong decrease of the lithium content, which is incompatible with stoichiometry of the precursor target [25,26,28]. Undoubtedly, the formation of only N_d and N_t species, as early studies suggested [1,21–24], would inevitably lead to a decrease in the Li/P ratio. It is also important to mention that, although in smaller content, as evidenced from ^{31}P NMR analyses, the presence of bridging oxygens forming $[O_3POPO_3]^{4-}$ pyrophosphate anions should be also associated to a decrease of lithium content in the film. That is probably the reason why the N_d/N parameter tend to deviate significantly from the

expected value of 50% in the case of low nitrogen content compositions (Table 2). Finally, the presence of marginal amounts of N_t species, although unlikely, cannot be completely ruled out.

Lastly, the local environment and mobility of Li^+ cations in LiPO(N) thin films were also probed by recording 1D ^{7}Li MAS NMR spectra. As shown in Figure 3, each spectrum exhibits a single central transition between energy levels $m_I = 1/2$ and $-1/2$ as well as spinning sidebands of the satellite transitions. Hence, at room temperature, Li^+ ions are mobile and exchange rapidly between the different Li sites during the acquisition of the ^{7}Li free-induction decay. As a result, a unique local environment is observed by NMR at near room temperature. As seen in Table 3, the isotropic chemical shift of ^{7}Li nuclei is higher for LiPON samples than for LiPO and increases with nitrogen content, which has not been reported so far. This observation reveals that nitridation decreases the coordination number of Li^+ ions [27]. This result is in close agreement with the increase of the dimerization of the amorphous structure suggested by the enhancement of the P_d/P ratio on nitrogen incorporation (Table 2). Furthermore, the width of the ^{7}Li central transition decreases with higher nitrogen content, evidencing that nitridation seems to enhance the mobility of Li^+ cations.

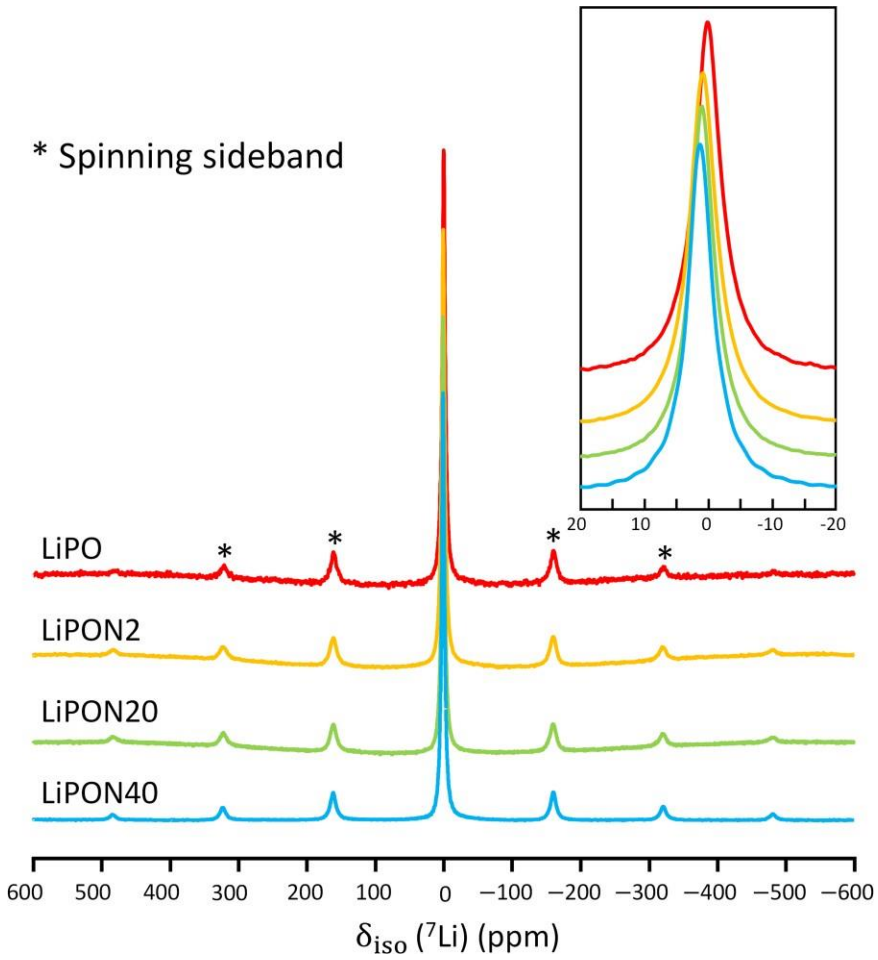

Figure 3 - 1D ^{7}Li MAS NMR spectra of LiPO, LiPON 2, LiPON20 and LiPON40 at 9.4 T with a MAS frequency of 25 kHz. The symbols * denote the spinning sidebands of the satellite transitions.

Table 3 - Isotropic chemical shifts and FWHM of ^{7}Li NMR signals of LiPO, LiPON2, LiPON20 and LiPON40 samples.

Sample	δ_{iso}(^{7}Li) (ppm)	FWHM (Hz)
LiPO	0.15	812
LiPON2	0.87	780
LiPON20	0.98	732
LiPON40	1.26	732

3.2 Electrical behavior of LiPON thin films

A preliminary analysis of the complex impedance response of LiPO(N) thin films reveals a very similar electrical behavior for all samples regardless the composition. Figure 4 depicts complex impedance plots for LiPO thin film synthesized under Ar and LiPON40 under N_2. The complex impedance plots of the LiPON2 and LiPON20 thin films also present the same typical impedance response (Figure S3). Overall, all thin films display an ion-conducting behavior characteristic of an amorphous material, typified by a straight and steep increase of the imaginary part of impedance (spike) at low frequency, jointly to the impedance response of the sample in higher frequencies (a single semi-circle). That low-frequency response is commonly denoted as a polarization effect and is due to the blockage of mobile ions at the interface between electrolyte and metallic electrodes [14,35]. Besides, the complex impedance data (Z*) have already been normalized regarding the shape factor of each sample (L/A, where L and A denotes the thickness of the electrolyte and electrodes area, respectively) to get the specific impedance Z^*_S ($Z^*_S = Z^*/(L/A)$), so that the impedance response of the samples can be directly compared. In this respect, the only apparent difference between LiPO (Figure 4a) and LiPON40 (Figure 4b) is the magnitude of their resistivity which can be read as the diameter of the semicircle (about 3 times higher for LiPO).

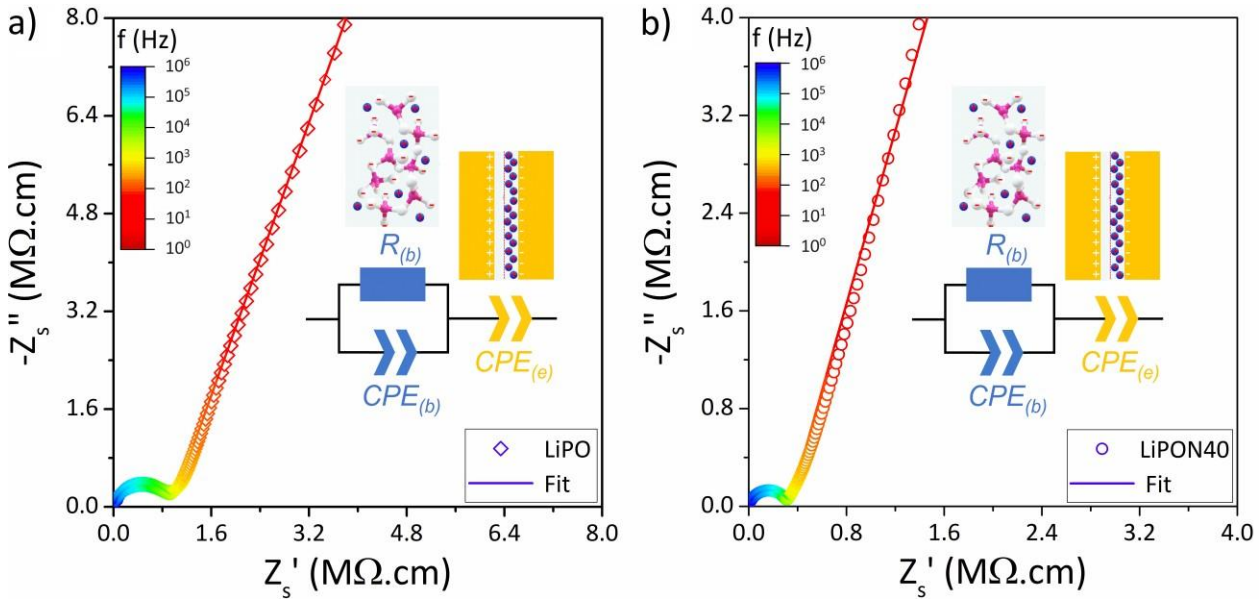

Figure 4 - Typical complex impedance plots of (a) LiPO and (b) LiPON40 thin films recorded at 298 K. The complex impedance data shown here have already been normalized regarding the shape factor of each sample in order to allow the direct comparison between samples. Insets show the schematics of the measurement cell and associated equivalent circuit used to fit the impedance data. Letter *R* and acronym *CPE* represent resistive and constant phase circuit elements, respectively, while subscripts b and e denote bulk and electrodes responses, respectively.

3.2.1 Ionic Conductivity

The impedance data were fitted applying a suitable equivalent circuit (Figure 4) to determine the resistivity and consequently the conductivity of the samples at distinct temperatures (Figure S4). Subsequently, the dependence of ionic conductivity on the inverse of temperature has been plotted applying the linearized form of the Arrhenius-like relation [36,37]:

$$\sigma T = \sigma_0 \, e^{\left(\frac{-E_a}{k_B T}\right)} \quad (1)$$

where k_B is the Boltzmann constant, T is the absolute temperature, σ_0 is the pre-exponential factor and E_a is the activation energy for ion conduction. Therefore, E_a can be accessed from the

slope of the linear fit in log (σT) vs $1/T$ plots shown in Figure 5. This slope slightly decreases for samples sputtered under N_2 flow comparatively to the LiPO sample, leading to a decrease of the activation energy from 0.575(2) eV for LiPO to 0.509(2) eV for LiPON40 (see Table 4). Consequently, the conductivity of the LiPON samples tends to increase with nitrogen incorporation, reaching up to 3.0(1) $\mu S.cm^{-1}$ at room temperature for LiPON40, which is around the most common value of conductivity reported in literature for the lithium phosphorus oxynitride with high nitrogen content [1,19,22,24]. Surprisingly, despite the lower nitrogen content, LiPON2 has an ionic conductivity (1.88 $\mu S.cm^{-1}$) and activation energy (0.527 eV) very similar to those of LiPON20 (1.89 $\mu S.cm^{-1}$ and 0.529 eV, respectively).

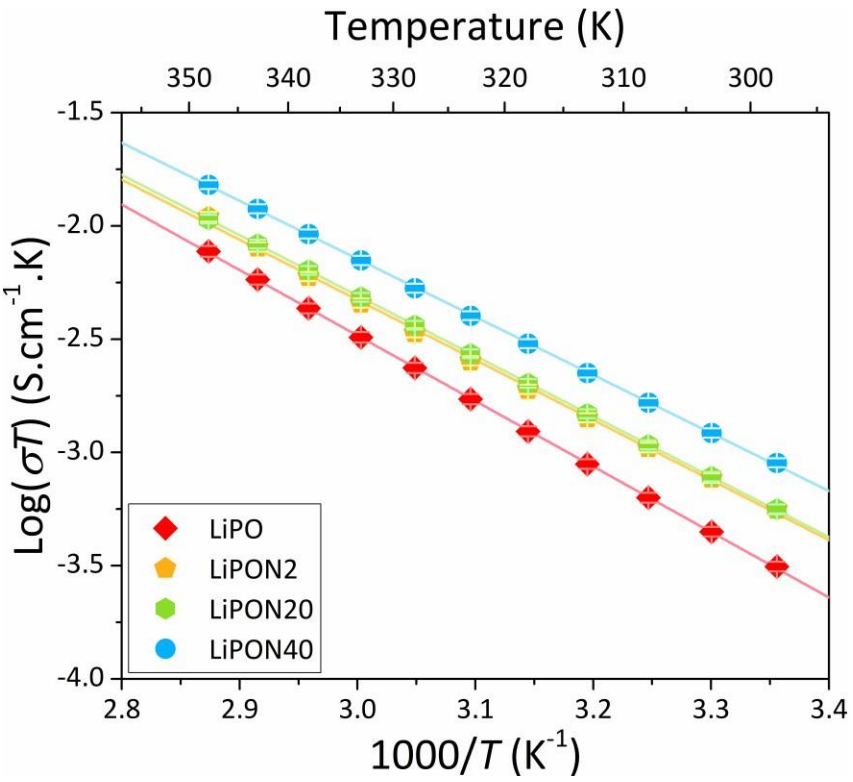

Figure 5 - Arrhenius-like plots of the ionic conductivity of LiPO(N) thin films sputtered under distinct nitrogen flow rate. Error bars are calculated from the relative errors of equivalent circuit parameters obtained by fitting impedance data and the random errors associated to the dimensions of the impedance cell.

Table 4 - Ionic conductivity at 298 K and activation energies of LiPON amorphous electrolytes with varied N content. Ionic conductivity uncertainties are estimated from the relative errors of equivalent circuit fit parameters and the random errors associated to the dimensions of the impedance while activation energy uncertainties are propagated from the linear fitting procedure.

Samples	Chemical Composition	σ	E_a
		$\mu S.cm^{-1}$	eV
LiPO	$Li_{2.9}PO_{4.3}$	1.05(5)	0.575(2)
LiPON2	$Li_{3.2}PO_{3.5}N_{0.25}$	1.88(9)	0.527(6)
LiPON20	$Li_{3.1}PO_{3.0}N_{0.57}$	1.89(9)	0.529(1)
LiPON40	$Li_{3.2}PO_{3.0}N_{0.68}$	3.0(1)	0.509(2)

3.2.2 Dielectric Permittivity

Likewise the ionic conductivity, the dielectric permittivity can be explored to gain understanding in the ionic transport of LiPO(N) solid electrolytes. The permittivity associated to the ionic-blocking effect is proportional to the concentration of charge carriers blocked at the electrolyte/electrode interphase [35,38]. Therefore, the concentration of mobile charge carriers (n_+) can be estimated based on the dielectric behavior of these amorphous electrolytes. A method based on the work of Coelho *et al.* [38] has been employed to determine n_+ of single-ion polymer electrolytes. More recently, Van-Jodin *et al.* have applied this methodology for LiPON thin film electrolytes [14]. The method consists in estimating the Debye length (L_D), which is the length scale of the electrostatic double layer, from the bulk (C_b) and electrodes (C_e) capacitances (Eq. 2) [14,35,38].

$$\frac{C_e}{C_b} = \frac{L}{2L_D} \quad (2)$$

Then, n_+ can be determined by applying Eq. 3 [14,35], with ε_r, being the relative permittivity of the bulk, determined from the bulk capacitance and the shape factor of the sample ($\varepsilon_r = C_b L/(\varepsilon_0 A)$).

$$n_+ = \frac{\varepsilon_r \varepsilon_0 T k_B}{(q^2 L_D^2)} \quad (3)$$

Electrode and bulk capacitances can be obtained by fitting the impedance data which in turn can be also converted in complex permittivity data [39]. Since the equivalent circuit used comprises non-ideal circuit elements, i.e., constant phase elements (CPE), the effective capacitances should be estimated based on the CPE fitting parameters Q and α [40], by applying the following equations:

$$C_b = (Q_b {R_b}^{1-\alpha_b})^{\frac{1}{\alpha_b}} \quad (5)$$

$$C_e = (Q_e {R_b}^{1-\alpha_e})^{\frac{1}{\alpha_e}} \quad (6)$$

where Q_b and α_b are the CPE fitting parameters associated to the bulk (CPE_b), whereas Q_e and α_e are the CPE fitting parameters associated to the electrodes (CPE_e) responses.

Figure 6 displays the dependence of the real part of permittivity on frequency for LiPO and LiPON40 electrolytes as well as the fitting curves applying the shown equivalent circuit. The dependence of the real part of relative permittivity on frequency of samples LiPON2 and LiPON20 thin films also present a similar dielectric behavior (Figure S5). The permittivity data presented have already been normalized regarding the shape factor of each sample and the vacuum permittivity (ε_0). The relative permittivity (ε_r) of the samples can be readily accessed in the high frequency plateau (around 30 for both samples at 298 K). On the other hand, the shift in permittivity between the high and the low-frequency plateau (about 1000 times) is proportional to the $L/(2L_D)$ ratio. Considering that the thicknesses of the LiPO(N) thin films prepared are in the order of one micrometer, the length of the Debye electrostatic double layer should be in the nanometric order.

To precisely determine L_D, the capacitances of bulk and electrodes are obtained from fitting the impedance data (Table S1). The obtained value of n_+ for LiPO and LiPON thin films are slightly dependent on the temperature and in the order of 10^{25} m^{-3}, which is about three orders of magnitude lower than the total lithium concentration in the film (~10^{28} m^{-3}). This result is consistent with early findings reported in literature that indicates that only a small share of Li^+ ions are involved in the conduction process [14,22].

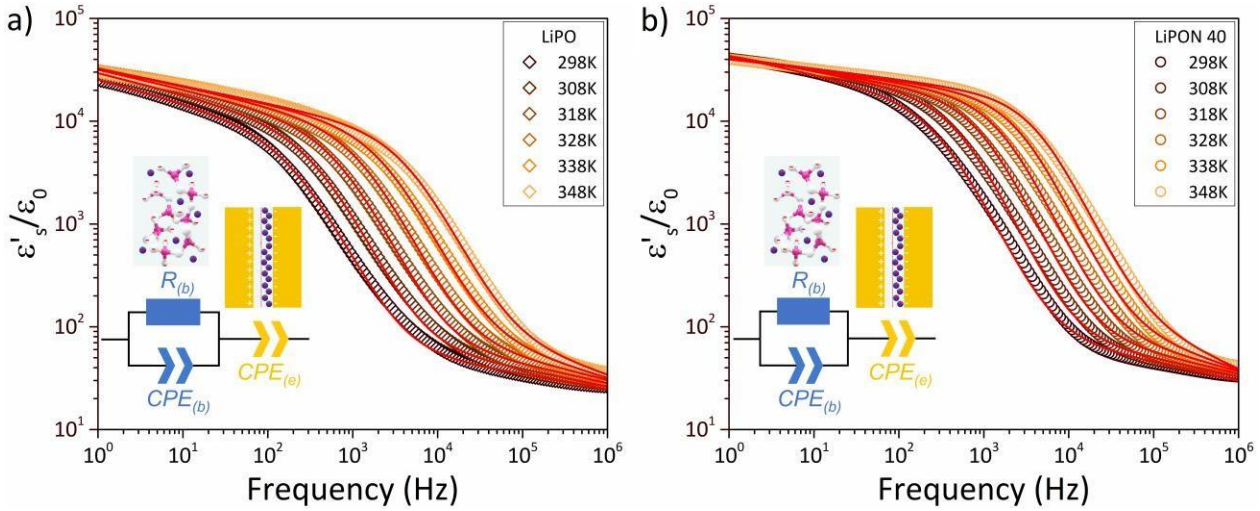

Figure 6 - Dependence of the real part of relative permittivity on frequency at different temperatures for samples (a) LiPO and (b) LiPON40 thin films. The permittivity data shown here have already been normalized regarding the shape factor of each sample and the vacuum permittivity. Insets shown the equivalent circuit used to fit the permittivity data, along with a schematic model of the LiPO(N) film samples and their interfaces with the gold electrodes. Letter *R* and acronym *CPE* represent respectively resistive and constant phase circuit elements, while subscript b and e denote bulk and electrodes responses, respectively.

3.3 The origin of the enhanced ionic conductivity

In order to identify the origin of the conductivity improvement combined to a decrease of the activation energy for nitrogen rich films, the ionic conductivity and dielectric permittivity data can

be correlated. Fast ion transport is usually achieved thanks to defects and energetically favored tracks for ion motion. Therefore, the objective here is to evaluate the temperature dependence of the concentration of effective charge carriers (n_+) and the diffusion coefficient (D) aiming to separate the energetic contributions related to defect formation from that of migration. These quantities are strictly related with the ionic conductivity (σ) by means of Nernst-Einstein equation [36,37]:

$$\sigma = \frac{n_+ D q^2}{H_R k_B T} \tag{6}$$

where q represents the charge associated to the mobile species which corresponds to the valence state multiplied by the elementary charge ($q = e$ for Li^+). H_R is the so-called Haven ratio and is related to the hopping mechanism, the mobile site coordination number, and the dimensionality of the conduction pathways [41]. The concentration of effective charge carriers, n_+, is often conditioned to ionic defect formation, which is itself governed by a thermally activated process that is expressed according to [36,37]:

$$n_+ = n\, e^{\left(\frac{\Delta S_F}{2k_B}\right)}\, e^{\left(-\frac{\Delta H_F}{2k_B T}\right)} \tag{7}$$

Here, n corresponds to the total concentration of the mobile species and ΔS_f and ΔH_f account for the entropic and enthalpic contributions to the defect formation, respectively. Similarly, the diffusion coefficient is also a thermoactivated process but in this case the enthalpy associated is proportional to the energetic barrier that needs to be overcome to displace the mobile species from one site to another. The temperature dependence of the diffusion coefficient is expressed by [36,37]:

$$D = \nu \lambda^2 e^{\left(\frac{\Delta S_m}{k_B}\right)}\, e^{\left(-\frac{\Delta H_m}{k_B T}\right)} \tag{8}$$

where ν is the ionic hopping attempt frequency, λ is the distance between two neighboring sites and ΔS_m and ΔH_m are respectively the entropic and the enthalpic terms related to the migration of the charged species.

Considering these two thermally activated processes, the previous presented Arrhenius-like equation (Eq. 1) can be rewritten based on fundamental terms by replacing D and n_+ in the Eq. 6 [36,37]:

$$\sigma = \frac{q^2 \lambda^2 \nu^2 n}{H_R k_B T} e^{\left(\frac{\Delta S_F/2 + \Delta S_m}{k_B}\right)} e^{\left(-\frac{\Delta H_F/2 + \Delta H_m}{k_B T}\right)} \quad (9)$$

Hence, Eq. 9 is equivalent to Eq. 1 if the pre-exponential term ($q^2\lambda^2\nu^2 ne^{(\Delta S_f/2k_B + \Delta S_m/k_B)}/H_R k_B$) is reduced to σ_0 and the enthalpic terms ($\Delta H_f/2 + \Delta H_m$) are directly associated to the activation energy (E_a). Consequently, the activation energy for ionic conductivity is actually constituted of two distinct contributions namely, migration and defect formation enthalpies. Their associate enthalpies are obtained employing the linearized form of Eqs. 7 and 8 to fit respectively n_+ (Figure 7a) and D (Figure 7b) data as function of the inverse temperature. The defect formation and migration enthalpies for each sample are shown in Figure 7c. Interestingly, the enthalpic contribution of defect formation for the overall activation energy is much less important than that of migration. Moreover, the observed variation of the enthalpy of defect formation as a function of the composition are within the associated error obtained from the linear fittings (Figure 7c). On the other hand, the enthalpy of migration slightly decreases with the enhancement of nitrogen flow, showing a variation of about 0.07 eV between LiPO and LiPON40 samples (Figure 7c). This is roughly the same difference found between activation energies of LiPO and LiPON40. Therefore, the difference between the activation energies caused by the increasing nitrogen content in LiPO(N) thin films is mainly associated to the energetic contribution related to the migration process. It is also worth noticing that the joint contributions of defect formation and migration

enthalpies ($\Delta H_f/2+ \Delta H_m$) are in good agreement with the activation energy values (Figure 7d) determined directly from conductivity data. This latter result reveals the self-consistence of the applied methodology. In theory, the intercepts on Figures 7a and b can be explored to access important transport parameter like *n* (Eq. 7) and λ (Eq. 8). However, the linearization of these equations results in unknown variables computed in the intercept parameter like ΔS_f (Eq. 7) and ΔS_m (Eq. 8) that precludes deeper analyses.

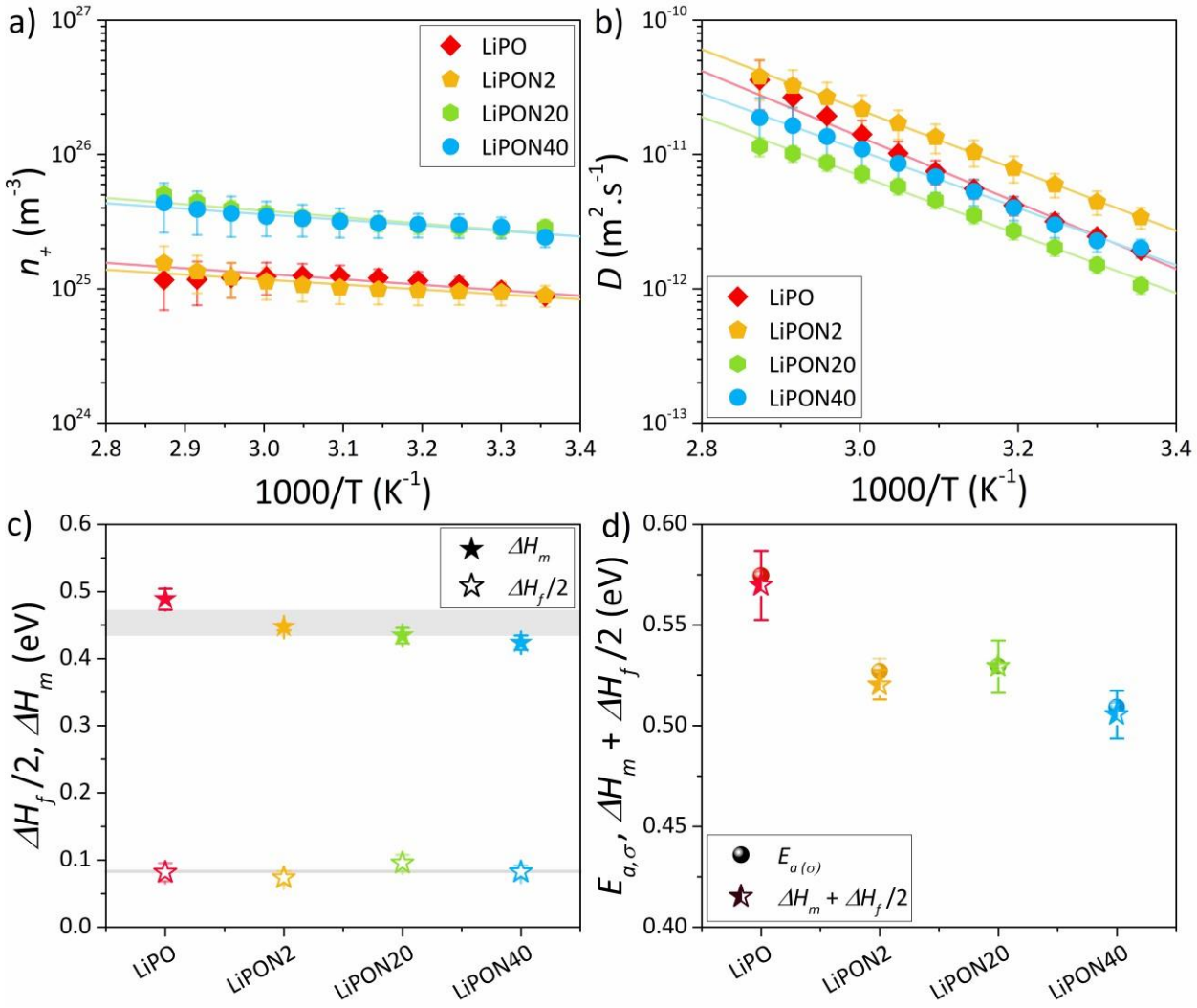

Figure 7 - Set of ionic transport parameters of LiPO(N) thin films represented by (a) the dependence of the concentration of effective charge carriers and (b) the diffusion coefficient on the inverse temperature, as well as (c) their corresponding enthalpies and (d) their joint contribution

comparatively to the activation energy obtained from conductivity data. Error bars in Figure 7a and b are propagated from the relative errors of the fitting parameters related to the employed equivalent circuit and the random errors associated to the dimensions of the impedance cell. Error bars in Figure 7c and d are propagated from the linear fitting procedure. Gray bands on Figure 7c depicts the difference between LiPO and LiPON samples considering uncertainties.

3.3.1 Impact of amorphization

Li^+ ion diffusion mechanisms in idealized γ-Li_3PO_4 crystal structure have been investigated by first principles calculations aiming to determine the migration energies by considering both vacancy and interstitial migration processes. The study suggests that the diffusion mechanism is more likely to occur via the concerted motion of an interstitial Li^+ ion and a neighboring Li^+ ion of the host lattice and leading to a total activation energy between 1 and 1.3 eV [42]. This range is in fair agreement with the one determined experimentally by EIS for crystalline γ-Li_3PO_4 [43]. The migration enthalpy is found in the range of 0.21-0.44 eV depending on the calculation method applied and the crystalline direction considered. On the other hand, the calculated defect formation enthalpy was found between 1.6 to 1.7 eV [42]. For all amorphous electrolytes experimentally investigated in our study, the defect formation enthalpy is about one order of magnitude lower (ΔH_f ~ 0.16 eV) than that calculated for crystalline γ-Li_3PO_4. The immense difference between ΔH_f of amorphous LiPO and its crystalline analog γ-Li_3PO_4 implies that the outstanding ionic conductivity of amorphous LiPO (about 12 orders of magnitude higher than γ-Li_3PO_4) is due a dramatic decrease of the enthalpy of defect formation which is inherent to its amorphous structure. This finding is supported by the evidence of structural disorder from the broad ^{31}P MAS NMR signal of LiPO amorphous electrolyte in contrast with a narrow isotropic signal of the NMR spectrum of crystalline γ-Li_3PO_4 [44]. Moreover, the recent work of Lacivita *et al.* [26] corroborates our findings, evidencing

that in simulated LiPO amorphous material, most of LiO_4 tetrahedra share edges with PO_4 units instead of corner as in crystalline γ-Li_3PO_4. This structural change would place Li^+ and P^{5+} in closer proximity to each other which would induce a destabilization of the Li sites in LiPO amorphous electrolytes facilitating the defect formation.

3.3.2 Effect of the nitridation

The local structural investigation by ^{31}P MAS NMR gives us insights to understand the role of nitrogen on the Li^+ transport in LiPON amorphous electrolytes. As the concentration of nitrogen in the thin films increases, an important increase of $[O_3PNPO_3]^{5-}$ dimers containing N_d sites is noted, which in turn follows the opposite trend of the migration enthalpy. Figure 8 depicts the evolution of the migration enthalpy (ΔH_m) and the concentration of $[O_3PNPO_3]^{5-}$ and $[O_3POPO_3]^{4-}$ dimers as well as the ratios N_d/N and P_d/P as a function of the nitrogen flow rate. The spotted correlation indicates that the increase of $[O_3PNPO_3]^{5-}$ dimers containing N_d sites is likely to be the main responsible for reducing the enthalpy of migration. Yet, the contribution of $[O_3POPO_3]^{4-}$, although in lower concentration, cannot be neglected. The concentration of both types of dimers subsumed by P_d/P ratio also follows the opposite trend of the migration enthalpy. Finally, the dependence of the N_d/N ratio on nitrogen content also correlates very well with the drop on the migration enthalpy. These findings are likewise supported by the recent study of Lacivita *et al.* [26], which emphasizes a weaker interaction of Li^+ ions with N_d sites than N_a sites. The same is true when comparing the interaction of Li^+ ions with N_d sites and with non-bridging oxygens from orthophosphate isolated tetrahedra (PO_4^{3-}) [26]. In summary, the increase of ionic conductivity caused by the nitrogen content in LiPON thin films should be mainly linked with the incorporation of nitrogen in the specific configuration N_d.

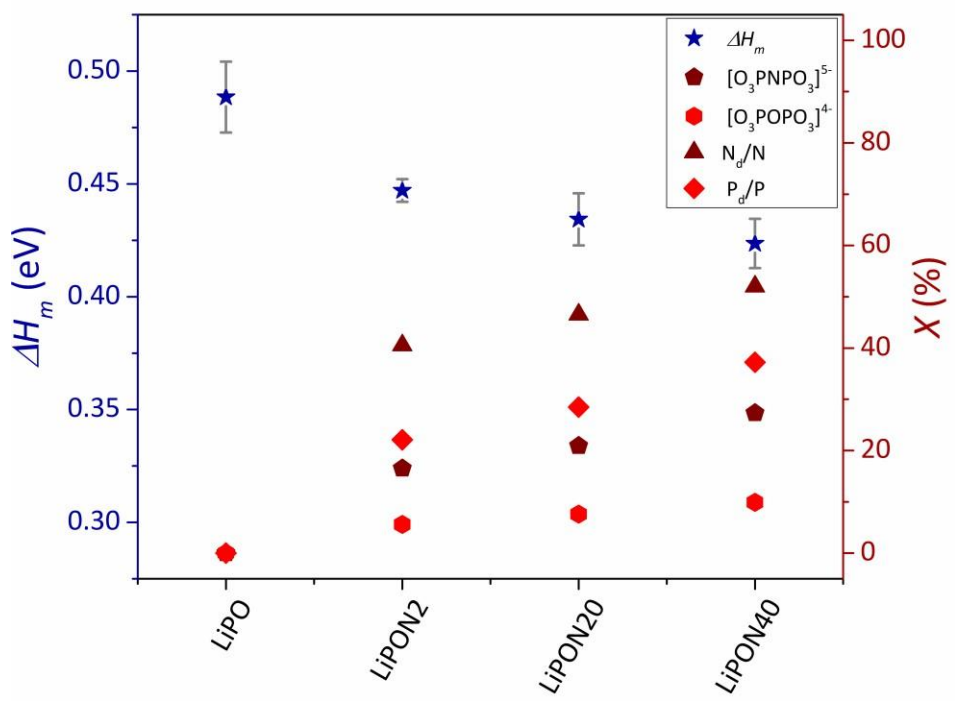

Figure 8 - Relationship between the migration enthalpy (ΔH_m) and the concentration of $[O_3PNPO_3]^{5-}$ and $[O_3POPO_3]^{4-}$ dimers as well as the ratios N_d/N and P_d/P as a function of the nitrogen content in LiPO(N) thin films. The concentration of PO_4^{3-} and PO_3N^{4-} isolated tetrahedral units are not included here because they do not present direct correlation with the drop of ΔH_m.

4 Conclusion

LiPON amorphous thin films were prepared by RF magnetron sputtering by varying the nitrogen content while maintaining the Li content constant. The resulting structure, once nitrogen is incorporated, was probed by 1D ^{31}P solid-state NMR analyses, which highlighted the presence of N_a and N_d local environments. This finding is in apparent contradiction with several structural studies based on XPS analyses of LiPON thin films that highlighted besides N_d, the presence of N_t local environments. Since XPS is an extreme surface technique, depth profiling XPS was employed for probing the structure down to the bulk. The comparison between XPS analyses in the surface and bulk reveals very distinct structures, leading to the conclusion that the N_t environment spotted in previous XPS studies is likely to be a product of surface degradation due to the intrinsic reactivity of LiPON thin films. Finally, a methodology based on impedance and permittivity analyses was applied to investigate the ionic transport and dissociate the enthalpic contribution of defect formation from that of migration. The main findings indicate that the enthalpy of defect formation in the synthesized amorphous thin films is astoundingly low compared to their crystalline counterpart. This finding emphasizes the impact of amorphization on the structure, increasing the disorder and placing a fraction of Li^+ in unstable sites that energetically favors the defect formation. Conversely, the enthalpy of migration is found to be the main contribution to the overall activation energy and considerably decreases with the incorporation of nitrogen. Therefore, the main impact of nitridation on ionic transport seems to be linked with the decrease of the energetic barrier related to migration, which is caused by the incorporation of bridging nitrogen species producing the partial dimerization of the resulting structure. Hence, not only the amount of nitrogen incorporated but also the local environment of nitrogen in the structure is critical to improve Li^+ ions migration and ultimately the ionic conductivity of LiPON thin films.

Associated Content

The Supporting Information is available free of charge on the ACS Publications website at DOI:

Schematic representation of the impedance measurement cell; High-resolution P 2p core level spectra of the surface and bulk of LiPON thin film samples; Typical complex impedance plots of LiPON2 and LiPON20 thin films recorded at 298 K; Complex impedance plots of LiPON40 thin film sample recorded at distinct temperatures; Dependence of the real part of relative permittivity on frequency at different temperatures for LiPON2 and LiPON20 thin film samples. Experimental results obtained from impedance data fitting and cell dimensions as well as the derived values of ionic conductivity, Debye length, relative permittivity, charge carrier concentration and diffusion coefficient.

Corresponding Author

Rafael Bianchini Nuernberg : *rafael.bianchini_nuernberg@bordeaux-inp.fr*

Univ. Bordeaux, CNRS, Bordeaux INP, ICMCB, UMR 5026, 33600 Pessac, France

Funding Sources

French National Research Agency (ANR) through the contract ANR-18-CE08-0015-01

Notes

The authors declare no competing financial interest.

Acknowledgments

The authors gratefully acknowledge the financial support of the French National Research Agency (ANR) through the contract ANR-18-CE08-0015-01 (ThinGlass) and from the French Alternative Energies and Atomic Energy Commission (CEA) for this work. We also want to thank Emmanuel Petit, from the Institute of the Condensed Matter Chemistry of Bordeaux (ICMCB, UMR 5026) for the ICP-OES chemical analyses and Dr Nithavong Cam, from the Plateforme Aquitaine de caractérisation des matériaux : UAR 3626 (PLACAMAT), for the EPMA chemical analyses. We would also want to thank Prof. Guillaume Wantz, from the Laboratoire de l'Intégration du Matériau au Système (IMS) for making the spin-coater available. Chevreul Institute (FR 2638), Ministère de l'Enseignement Supérieur et de la Recherche, Hauts-de-France Region, and FEDER are acknowledged for supporting and funding partially this work. Financial support from the IR INFRANALYTICS FR2054 CNRS for conducting the research is gratefully acknowledged.

References

(1) Bates, J. B.; Dudney, N. J.; Gruzalski, G. R.; Zuhr, R. A.; Choudhury, A.; Luck, C. F.; Robertson, J. D. Fabrication and Characterization of Amorphous Lithium Electrolyte Thin Films and Rechargeable Thin-Film Batteries. J Power Sources 1993, 43 (1–3), 103–110. https://doi.org/10.1016/0378-7753(93)80106-Y.

(2) Bates, J. B.; Dudney, N. J.; Gruzalski, G. R.; Zuhr, R. A.; Choudhury, A.; Luck, C. F.; Robertson, J. D. Electrical Properties of Amorphous Lithium Electrolyte Thin Films. Solid State Ion 1992, 53–56 (PART 1), 647–654. https://doi.org/10.1016/0167-2738(92)90442-R.

(3) Zhu, Z.; Kan, R.; Hu, S.; He, L.; Hong, X.; Tang, H.; Luo, W. Recent Advances in High-Performance Microbatteries: Construction, Application, and Perspective. Small 2020, 16 (39), 2003251. https://doi.org/10.1002/smll.202003251.

(4) Bates, J. B.; Dudney, N. J.; Lubben, D. C.; Gruzalski, G. R.; Kwak, B. S.; Yu, X.; Zuhr, R. A. Thin-Film Rechargeable Lithium Batteries. J Power Sources 1995, 54 (1), 58–62. https://doi.org/10.1016/0378-7753(94)02040-A.

(5) Bates, J. B.; Dudney, N. J.; Neudecker, B.; Ueda, A.; Evans, C. D. Bates, J. B., Dudney, N. J., Neudecker, B., Ueda, A., & Evans, C. D. (2000). Thin-Film Lithium and Lithium-Ion Batteries. Solid State Ionics, 135(1-4), 33–45. https://doi.org/10.1016/S0167-2738(00)00327-1

(6) Vieira, E. M. F.; Ribeiro, J. F.; Silva, M. M.; Barradas, N. P.; Alves, E.; Alves, A.; Correia, M. R.; Goncalves, L. M. Electrical Insulation Properties of RF-Sputtered LiPON Layers towards Electrochemical Stability of Lithium Batteries. J Phys D Appl Phys 2016, 49 (48). https://doi.org/10.1088/0022-3727/49/48/485301.

(7) Ko, J.; Cho, D. H.; Kim, D.-J.; Yoon, Y. S. Suppression of Formation of Lithium Dendrite via Surface Modification by 2-D Lithium Phosphorous Oxynitride as a Highly Stable Anode for Metal Lithium Batteries. J Alloys Compd 2020, 845, 156280. https://doi.org/10.1016/j.jallcom.2020.156280.

(8) Ioanniti, M. M.; Hu, F.; Tenhaeff, W. E. Energy-Dense Li Metal Anodes Enabled by Thin Film Electrolytes. Journal of Vacuum Science & Technology A 2020, 38 (6), 060801. https://doi.org/10.1116/6.0000430.

(9) Li, J.; Dudney, N. J.; Nanda, J.; Liang, C. Artificial Solid Electrolyte Interphase to Address the Electrochemical Degradation of Silicon Electrodes. ACS Appl Mater Interfaces 2014, 6 (13), 10083–10088. https://doi.org/10.1021/am5009419.

(10) Zhu, Y.; He, X.; Mo, Y. Origin of Outstanding Stability in the Lithium Solid Electrolyte Materials: Insights from Thermodynamic Analyses Based on First-Principles Calculations. ACS Appl Mater Interfaces 2015, 7 (42), 23685–23693. https://doi.org/10.1021/acsami.5b07517.

(11) Schwöbel, A.; Hausbrand, R.; Jaegermann, W. Interface Reactions between LiPON and Lithium Studied by In-Situ X-Ray Photoemission. Solid State Ion 2015, 273, 51–54. https://doi.org/10.1016/j.ssi.2014.10.017.

(12) Cheng, D.; Wynn, T. A.; Wang, X.; Wang, S.; Zhang, M.; Shimizu, R.; Bai, S.; Nguyen, H.; Fang, C.; Kim, M. cheol; Li, W.; Lu, B.; Kim, S. J.; Meng, Y. S. Unveiling the Stable Nature of the Solid Electrolyte Interphase between Lithium Metal and LiPON via Cryogenic Electron Microscopy. Joule 2020, 4 (11), 2484–2500. https://doi.org/10.1016/j.joule.2020.08.013.

(13) Browning, K. L.; Westover, A. S.; Browning, J. F.; Doucet, M.; Sacci, R. L.; Veith, G. M. In Situ Measurement of Buried Electrolyte-Electrode Interfaces for Solid State Batteries with Nanometer Level Precision. ACS Energy Lett 2023, 8 (4), 1985–1991. https://doi.org/10.1021/acsenergylett.3c00488.

(14) Le Van-Jodin, L.; Ducroquet, F.; Sabary, F.; Chevalier, I. Dielectric Properties, Conductivity and Li+ Ion Motion in LiPON Thin Films. Solid State Ion 2013, 253, 151–156. https://doi.org/10.1016/j.ssi.2013.09.031.

(15) Mo, F.; Ruan, J.; Sun, S.; Lian, Z.; Yang, S.; Yue, X.; Song, Y.; Zhou, Y.; Fang, F.; Sun, G.; Peng, S.; Sun, D. Inside or Outside: Origin of Lithium Dendrite Formation of All Solid-State Electrolytes. Adv Energy Mater 2019, 9 (40), 1902123. https://doi.org/10.1002/aenm.201902123.

(16) Tian, H.-K.; Xu, B.; Qi, Y. Computational Study of Lithium Nucleation Tendency in $Li_7La3Zr_2O_{12}$ (LLZO) and Rational Design of Interlayer Materials to Prevent Lithium Dendrites. J Power Sources 2018, 392, 79–86. https://doi.org/10.1016/j.jpowsour.2018.04.098.

(17) Grady, Z. A.; Wilkinson, C. J.; Randall, C. A.; Mauro, J. C. Emerging Role of Non-Crystalline Electrolytes in Solid-State Battery Research. Frontiers in Energy Research. 2020, pp 1–23. https://doi.org/10.3389/fenrg.2020.00218.

(18) Han, F.; Westover, A. S.; Yue, J.; Fan, X.; Wang, F.; Chi, M.; Leonard, D. N.; Dudney, N. J.; Wang, H.; Wang, C. High Electronic Conductivity as the Origin of Lithium Dendrite Formation within Solid Electrolytes. Nat Energy 2019, 4 (3), 187–196. https://doi.org/10.1038/s41560-018-0312-z.

(19) Li, J.; Ma, C.; Chi, M.; Liang, C.; Dudney, N. J. Solid Electrolyte: The Key for High-Voltage Lithium Batteries. Adv Energy Mater 2015, 5 (4). https://doi.org/10.1002/aenm.201401408.

(20) Hamon, Y.; Douard, A.; Sabary, F.; Marcel, C.; Vinatier, P.; Pecquenard, B.; Levasseur, A. Influence of Sputtering Conditions on Ionic Conductivity of LiPON Thin Films. Solid State Ion 2006, 177 (3–4), 257–261. https://doi.org/10.1016/j.ssi.2005.10.021.

(21) Nimisha, C. S.; Rao, K. Y.; Venkatesh, G.; Rao, G. M.; Munichandraiah, N. Sputter Deposited LiPON Thin Films from Powder Target as Electrolyte for Thin Film Battery

Applications. Thin Solid Films 2011, 519 (10), 3401–3406. https://doi.org/10.1016/j.tsf.2011.01.087.

(22) Fleutot, B.; Pecquenard, B.; Martinez, H.; Letellier, M.; Levasseur, A. Investigation of the Local Structure of LiPON Thin Films to Better Understand the Role of Nitrogen on Their Performance. Solid State Ion 2011, 186 (1), 29–36. https://doi.org/10.1016/j.ssi.2011.01.006.

(23) Su, Y.; Falgenhauer, J.; Polity, A.; Leichtweiß, T.; Kronenberger, A.; Obel, J.; Zhou, S.; Schlettwein, D.; Janek, J.; Meyer, B. K. LiPON Thin Films with High Nitrogen Content for Application in Lithium Batteries and Electrochromic Devices Prepared by RF Magnetron Sputtering. Solid State Ion 2015, 282, 63–69. https://doi.org/10.1016/j.ssi.2015.09.022.

(24) Suzuki, N.; Shirai, S.; Takahashi, N.; Inaba, T.; Shiga, T. A Lithium Phosphorous Oxynitride (LiPON) Film Sputtered from Unsintered Li_3PO_4 Powder Target. Solid State Ion 2011, 191 (1), 49–54. https://doi.org/10.1016/j.ssi.2011.04.001.

(25) Muñoz, F. Comments on the Structure of LiPON Thin-Film Solid Electrolytes. J Power Sources 2012, 198, 432–433. https://doi.org/10.1016/j.jpowsour.2011.09.009.

(26) Lacivita, V.; Artrith, N.; Ceder, G. Structural and Compositional Factors That Control the Li-Ion Conductivity in LiPON Electrolytes. Chemistry of Materials 2018, 30 (20), 7077–7090. https://doi.org/10.1021/acs.chemmater.8b02812.

(27) Marple, M. A. T.; Wynn, T. A.; Cheng, D.; Shimizu, R.; Mason, H. E.; Meng, Y. S. Local Structure of Glassy Lithium Phosphorus Oxynitride Thin Films: A Combined Experimental and Ab Initio Approach. Angewandte Chemie - International Edition 2020, 59 (49), 22185–22193. https://doi.org/10.1002/anie.202009501.

(28) Lacivita, V.; Westover, A. S.; Kercher, A.; Phillip, N. D.; Yang, G.; Veith, G.; Ceder, G.; Dudney, N. J. Resolving the Amorphous Structure of Lithium Phosphorus Oxynitride (LiPON). J Am Chem Soc 2018, 140 (35), 11029–11038. https://doi.org/10.1021/jacs.8b05192.

(29) Li, J.; Lai, W. Structure and Ionic Conduction Study on Li_3PO_4 and LiPON (Lithium Phosphorous Oxynitride) with the Density-Functional Tight-Binding (DFTB) Method. Solid State Ion 2020, 351 (January), 115329. https://doi.org/10.1016/j.ssi.2020.115329.

(30) Bayzou, R.; Trébosc, J.; Landry, A.-K.; Nuernberg, R. B.; Cras, B. P.-L.; Cras, F. Le; Pourpoint, F.; Lafon, O. Identification of Phosphorus Sites in Amorphous LiPON Thin Film by Observing Internuclear Proximities. Journal of Magnetic Resonance 2023, 354, 107530. https://doi.org/10.1016/j.jmr.2023.107530.

(31) Massiot, D.; Fayon, F.; Capron, M.; King, I.; Le Calvé, S.; Alonso, B.; Durand, J.-O.; Bujoli, B.; Gan, Z.; Hoatson, G. Modelling One- and Two-Dimensional Solid-State NMR Spectra. Magnetic Resonance in Chemistry 2002, 40 (1), 70–76. https://doi.org/10.1002/mrc.984.

(32) Wang, B.; Chakoumakos, B. C.; Sales, B. C.; Kwak, B. S.; Bates, J. B. Synthesis, Crystal Structure, and Ionic Conductivity of a Polycrystalline Lithium Phosphorus Oxynitride with the γ-Li_3PO_4 Structure. J Solid State Chem 1995, 115 (2), 313–323. https://doi.org/10.1006/jssc.1995.1140.

(33) Guille, É.; Vallverdu, G.; Baraille, I. First-Principle Calculation of Core Level Binding Energies of $Li_xPO_yN_z$ Solid Electrolyte. Journal of Chemical Physics 2014, 141 (24). https://doi.org/10.1063/1.4904720.

(34) Guille, É.; Vallverdu, G.; Tison, Y.; Bégué, D.; Baraille, I. Possible Existence of a Monovalent Coordination for Nitrogen Atoms in $Li_xPO_yN_z$ Solid Electrolyte: Modeling of X-Ray Photoelectron Spectroscopy and Raman Spectra. Journal of Physical Chemistry C 2015, 119 (41), 23379–23387. https://doi.org/10.1021/acs.jpcc.5b08427.

(35) Klein, R. J.; Zhang, S.; Dou, S.; Jones, B. H.; Colby, R. H.; Runt, J. Modeling Electrode Polarization in Dielectric Spectroscopy: Ion Mobility and Mobile Ion Concentration of Single-Ion Polymer Electrolytes. Journal of Chemical Physics 2006, 124 (14). https://doi.org/10.1063/1.2186638.

(36) Rodrigues, A. C. M.; Nascimento, M. L. F.; Bragatto, C. B.; Souquet, J. L. Charge Carrier Mobility and Concentration as a Function of Composition in $AgPO_3$-AgI Glasses. Journal of Chemical Physics 2011, 135 (23). https://doi.org/10.1063/1.3666835.

(37) Nuernberg, R. B. Numerical Comparison of Usual Arrhenius-Type Equations for Modeling Ionic Transport in Solids. Ionics (Kiel) 2020, 26 (5), 2405–2412. https://doi.org/10.1007/s11581-019-03243-7.

(38) Coelho, R. On the Static Permittivity of Dipolar and Conductive Media - an Educational Approach. J Non Cryst Solids 1991, 131–133 (PART 2), 1136–1139. https://doi.org/10.1016/0022-3093(91)90740-W.

(39) Piarristeguy, A.; Nuernberg, R.; Jouglard, D.; Ramonda, M.; Arinero, R.; Pradel, A.; Neyret, M. High-Resolution Electrical Characterization of RuO_2-Borosilicate Glass Composites. J Alloys Compd 2021, 876, 160123. https://doi.org/10.1016/j.jallcom.2021.160123.

(40) Hirschorn, B.; Orazem, M. E.; Tribollet, B.; Vivier, V.; Frateur, I.; Musiani, M. Determination of Effective Capacitance and Film Thickness from Constant-Phase-Element Parameters. Electrochim Acta 2010, 55 (21), 6218–6227. https://doi.org/10.1016/j.electacta.2009.10.065.

(41) Isard, J. O. The Haven Ratio in Glasses. J Non Cryst Solids 1999, 246 (1–2), 16–26. https://doi.org/10.1016/S0022-3093(99)00036-8.

(42) Du, Y. A.; Holzwarth, N. A. W. Mechanisms of Li+ Diffusion in Crystalline γ- and β-Li_3PO_4 Electrolytes from First Principles. Phys Rev B 2007, 76 (17), 174302. https://doi.org/10.1103/PhysRevB.76.174302.

(43) Ivanov-Shitz, A. K.; Kireev, V. V.; Mel'nikov, O. K.; Demianets, L. N. Growth and Ionic Conductivity of γ-Li_3PO_4. Crystallography Reports 2001, 46 (5), 864–867. https://doi.org/10.1134/1.1405880.

(44) Stallworth, P. E.; Vereda, F.; Greenbaum, S. G.; Haas, T. E.; Zerigian, P.; Goldner, R. B. Solid-State NMR Studies of Lithium Phosphorus Oxynitride Films Prepared by Nitrogen Ion Beam-Assisted Deposition. J Electrochem Soc 2005, 152 (3), A516. https://doi.org/10.1149/1.1856922.

Table of Contents Graphic